

Impact of Finite Phonon Lifetimes on the Spin Dynamics of Single-Molecule Magnets

Rizwan Nabi,^a Jon G. C. Kragsskow,^a Jakob K. Staab,^a Daniel Reta,^{a,b,c,d} Jonathan M. Skelton^{a,*} and Nicholas F. Chilton^{a,*}

^a Department of Chemistry, University of Manchester, Manchester M13 9PL, UK

^b Faculty of Chemistry, The University of the Basque Country UPV/EHU, 20018, Donostia, Spain

^c Donostia International Physics Center (DIPC), Ikerbasque, 20018, Donostia, Spain

^d IKERBASQUE, Basque Foundation for Science, 48013, Bilbao, Spain

Email: jonathan.skelton@manchester.ac.uk, nicholas.chilton@manchester.ac.uk

Abstract

The development of single-molecule magnets (SMMs) for information storage and processing relies on compounds with long spin lifetimes, and thus requires an understanding of the spin-phonon coupling. The phonon bath itself has a central role in these interactions, and hence knowledge of the impact of the intrinsic phonon lifetimes is crucial. Here we address this challenge by performing fully *ab initio* calculations of the phonon linewidths for a molecular crystal of a high-performance SMM. We find that the commonly assumed Born-Markov approximation is justified as phonon dynamics are orders of magnitude faster than the spin dynamics, and that employing *ab initio*-calculated linewidths in spin-dynamics simulations are secondary to employing a dense numerical sampling of the phonon modes in reciprocal space.

Introduction

Single-molecule magnets (SMMs) are molecules that possess magnetic bistability and show magnetic memory effects at low temperatures in the absence of long-range order.^{1,2} SMMs are proposed as platforms for nanoscale information storage,³ quantum information processing,^{4,5} and molecular spintronics.⁶ One of the main goals has been pursuit of ever-slower spin dynamics to ensure that magnetic memory and quantum phase coherence remain for as long as possible, which are key challenges for practical applications to data storage and in quantum computing, respectively. The timescale for magnetic memory, τ , is set by the interactions of the molecule with its environment and is mediated by the vibrational modes (the phonons in the solid-state),^{7,8} and the same interactions limit the timescale of quantum coherence when other mechanisms are suppressed.⁹

Loss of magnetic memory in SMMs, also known as magnetic reversal or magnetic relaxation, occurs through different processes dictated by the spin dynamics. Single-phonon interactions lead to magnetic relaxation *via* the Orbach mechanism, for which the characteristic time has an exponential temperature dependence $\tau = \tau_0 \exp(U_{\text{eff}}/k_B T)$ with an attempt time τ_0 and an energy barrier U_{eff} . In recent “high-temperature” SMMs the Orbach process has been found to be driven by high-energy optic phonons.^{10,11} At lower temperatures, the Orbach mechanism is suppressed since the populations of high-energy phonons are very low, and the spin dynamics are instead dominated by two-phonon Raman mechanisms driven by low-energy (pseudo-)acoustic phonons. This generally leads to a power-law temperature dependence of τ in the range of T^{-1} to T^{-7} ,¹² although the appearance of a fixed power-law dependence is the result of the small temperature window where the process is isolated.¹³ There are two forms of the Raman mechanism, which arise from their derivation using time-dependent perturbation theory:¹⁴ the Raman-I mechanism (first-order in spin-phonon coupling, second-order in time) does not depend on the magnitude of an external magnetic field,¹⁵ while the Raman-II mechanism (second-order in spin-phonon coupling, first-order in time) has a quadratic dependence on the field.¹³ There are other mechanisms pertinent to the spin dynamics of SMMs, such as the Direct and Quantum Tunnelling of the Magnetisation (QTM) mechanisms,¹ which are not discussed here as they are not relevant in zero magnetic field and are not primarily activated by phonons, respectively.

Among the current best-performing SMMs, magnetic hysteresis has been observed as high as 80 K for $[\text{Dy}(\text{Cp}^*)(\text{Cp}^i\text{Pr}_5)][\text{B}(\text{C}_6\text{F}_5)_4]$ ($\text{Cp}^* =$ pentamethyl-cyclopentadienyl),¹⁶ and more recently for the mixed-valence $\text{Cp}^{i\text{Pr}5}\text{DyI}_3\text{DyCp}^{i\text{Pr}5}$ ($\text{Cp}^{i\text{Pr}5} =$ pentaisopropyl-cyclopentadienyl) featuring strong magnetic exchange coupling mediated by the Ln-Ln half- σ bond.¹⁷ In both cases, a large axial magnetic anisotropy is imposed by the cyclopentadienyl ligands, leading to large U_{eff} values and slow Orbach relaxation. For $[\text{Dy}(\text{Cp}^{\text{ttt}})_2][\text{B}(\text{C}_6\text{F}_5)_4]$ ($\text{Cp}^{\text{ttt}} =$ C₅H₂-1,2,4-^tBu)¹⁰ it has been demonstrated that the slow spin dynamics in the Raman regime result from a separation in energy between very high-energy optical phonons, due to the conjugated five-membered rings being the only ligands in the first coordination sphere, and low-energy pseudo-acoustic phonons due to the soft intermolecular potential energy.¹³ Variation of the cyclopentadienyl substituents can have a significant effect on the spin dynamics^{10,16,18} since it impacts both the magnetic anisotropy and vibrational spectrum¹⁹ – yet, control of the spin dynamics through chemical modification remains an open challenge for the design of improved

SMMs. Given the vastness of the chemical space, strategies employing machine learning are likely to be particularly promising.²⁰

To this end, a number of research groups have recently started to develop *ab initio* methods for calculating molecular spin-phonon coupling and modelling spin dynamics.^{19,21,22} This area started to grow rapidly with reports from three separate groups in 2017. Lunghi *et al.* examined the spin-phonon coupling and spin dynamics in the Fe(II) SMM [(tpa^{Ph})Fe]⁻ (H₃tpa^{Ph} = tris((5-phenyl-1H-pyrrol-2-yl)methyl)amine) and showed that phonon dissipation and anharmonicity were important in governing under-barrier relaxation processes.²³ Escalera-Moreno *et al.* explored the spin-phonon coupling in the Cu(II) molecular qubit [Cu(mnt)₂]²⁻ (mnt²⁻ = 1,2-dicyanoethylene-1,2-dithiolate) and found that the lowest-energy intramolecular vibrational modes were of most concern for mitigating quantum decoherence.²¹ Finally, work in our group examined the spin-phonon coupling and spin dynamics of [Dy(Cp^{III})₂][B(C₆F₅)₄] to establish that relaxation in the Orbach regime was due to high-energy optic modes, and that substitution of the Cp-bound C-H groups could have a significant impact on the magnetic memory timescales.¹⁰ [This prediction was later confirmed in work by the Layfield and Long and Harvey groups,^{16,18} though the origin of the improved performance was more nuanced than originally thought.¹⁹]

Our approach to *ab initio* spin dynamics has hitherto been to examine spin-phonon coupling in the gas-phase, which was necessarily limited to single-phonon processes as the rotational and translational modes are zero energy by construction and there are thus no low-energy phonons to mediate the two-phonon Raman mechanisms.^{19,24,25} On the other hand, Lunghi *et al.* considered the solid-state from the start, initially focussing on the Γ -point phonon modes^{23,26} and more recently expanding this to an integration over the first Brillouin zone to obtain the first fully-*ab initio* simulations of the Raman spin dynamics in an SMM.²⁷ In the absence of a full solid-state calculation in our previous *ab initio* studies, we used a phonon linewidth function to generate a “pseudo” density of states (pseudo-DoS) for modelling single-phonon processes, based on the discrete set of modes obtained from a gas-phase harmonic calculation. This linewidth approximates the dispersion of the phonon energy as a function of wavevector, which is naturally included in solid-state calculations with appropriate reciprocal-space sampling. However, in reality, phonons have finite lifetimes τ_p due to a variety of scattering processes, which means that the intrinsic linewidths $\Gamma = \hbar/\tau_p$ (where Γ is the full-width-at-half-maximum (FWHM) Lorentzian linewidth) may also vary intricately as a function of energy and wavevector.²⁸ Disregarding scattering from structural or magnetic impurities and

features such as crystallite boundaries, the leading contributor to finite phonon lifetimes are interactions with other phonons, of which the lowest-order are three-phonon scattering processes.²⁸ The τ_p depend on the nature of the modes, their energy, and their wavevectors, and are intrinsically temperature-dependent through the populations of the modes involved in the scattering processes. In our own work, we have previously treated the linewidths as a parameter.¹⁹ On the other hand, the 2017 study by Lunghi *et al.* suggested that the phonon lifetimes would play a crucial role in the magnetic relaxation processes, and proposed a simplified model for an effective phonon linewidth based on the NVT canonical ensemble (Equation 1).²³

$$\Gamma_j = 2\hbar\omega_j e^{\frac{\hbar\omega_j}{2k_B T}} / \left(e^{\frac{\hbar\omega_j}{k_B T}} - 1 \right)$$

(Equation 1)

While the question of the phonon linewidths may sound trivial, they can affect magnetic relaxation rates by orders of magnitude, and a proper treatment is therefore a significant question for research in this field.

Anticipating that *ab initio* spin-phonon coupling calculations will continue to play an important role in studying SMMs, we sought to directly investigate the phonon linewidths in molecular solids and to assess their impact on the spin dynamics. In this work, we approach this by calculating the phonon linewidths of the high performance Dy(III) SMM, [Dy(bbpen)Br] (**1**),²⁹ using a perturbative approach based on the third-order (anharmonic) force constants.²⁸ This system was chosen because of its small unit-cell size, relatively high-symmetry space group ($C222_1$), and excellent SMM performance. CASSCF-SO calculations were performed to quantify the spin-phonon coupling for the full set of phonon modes on a series of Brillouin-zone sampling grids. We then calculated the magnetic relaxation rates including the phonon dispersion and *ab initio* temperature-dependent linewidths, providing the least approximate model for the molecular spin dynamics to date. Our results show that the phonon linewidths are highly energy- and wavevector-dependent, with the FWHM varying between 0.1 – 40 cm^{-1} in **1** at 300 K. However, we find that the magnetic relaxation rates are relatively insensitive to the linewidths, provided a sufficient integration of the Brillouin zone is performed, with similar results obtained using a fixed linewidth, the function proposed by Lunghi *et al.* (Equation 1), or the *ab initio* temperature-dependent linewidths.

Methods

Lattice-dynamics calculations were performed on the primitive cell of **1**, obtained from the Cambridge Structural Database (CCDC: 1416543), using periodic density-functional theory (DFT) as implemented in VASP 5.4.4.^{30–33} The PBE functional³⁴ with the DFT-D3 semi-empirical dispersion correction³⁵ was employed to model the electron exchange and correlation. The ion cores were modelled with projector augmented-wave (PAW) pseudopotentials,^{36,37} with a 4f-in-core potential for Dy(III) used to avoid issues with treating the strongly-correlated f electrons on the lanthanide using semi-local DFT. We used a plane wave basis set with an energy cutoff of 800 eV at the Γ point to model the valence electronic structure, with both parameters determined *via* explicit convergence testing. The cell content and parameters of **1** were optimised starting from the primitive cell of the published X-ray structure, with the atomic positions (128 atoms), unit cell parameters and unit cell volume allowed to relax, to tight tolerances of 10^{-8} eV on the electronic total energy and 10^{-2} eV \AA^{-1} on the forces. Lattice-dynamics calculations were performed using the supercell finite-difference method implemented in the Phonopy³⁸ and Phono3py²⁸ codes. A $2 \times 2 \times 1$ supercell with 512 atoms was employed to determine the second-order force constants in Phonopy,³⁸ which was required to remove imaginary modes at the Y and T wavevectors in the calculated phonon dispersion. The third-order force constants for the primitive cell were determined using Phono3py,²⁸ where the phonon frequencies and linewidths were then evaluated on uniform $2 \times 2 \times 2$, $3 \times 3 \times 3$, $4 \times 4 \times 4$ and $5 \times 5 \times 5$ q -point grids using Fourier interpolation.

We adapted our established protocol for modelling molecular spin dynamics¹⁹ to take into account the phonon modes in the crystalline phase. The set of phonon wavevectors q on a Γ -centred q -point sampling grid with $q_1 \times q_2 \times q_3$ subdivisions are commensurate with a $q_1 \times q_2 \times q_3$ supercell expansion in real space (i.e. the supercell is of the correct size to contain an integer number of phonon wavelengths for all the q on the sampling grid). Given a q -point grid, the spin-phonon coupling must be evaluated for the corresponding supercell. We first take the optimised unit cell and generate the required supercell. We then take each unique molecule in the supercell (expanded to contain complete molecules) and perform a gas-phase DFT calculation using Gaussian 09d,³⁹ with Dy substituted by Y to avoid a multiconfigurational ground state, and determine the atomic charges required to reproduce the external molecular electrostatic potential using the CHELPG method⁴⁰ (PBE functional,³⁴ Stuttgart RSC 1997 ECP for Y^{41–43} and the cc-pVDZ basis sets for all other atoms⁴⁴). A periodic shift is then applied to place a single molecule of **1** at the centre of the supercell, and the remaining atoms are

replaced by the atomic point charges. The molecule is then treated with a state-average complete active space self-consistent field spin-orbit (SA-CASSCF-SO) calculation in OpenMolcas.⁴⁵

We consider 18 $S = 5/2$ states (6H and 6F terms) in a 9-in-7 active space ($4f^9$ configuration) using the second-order Douglas-Kroll-Hess relativistic decoupling,⁴⁶ the Cholesky “atomic compact” resolution of the identity method for approximating the two-electron integrals,⁴⁷ and ANO-RCC basis sets for all atoms (VTZP for Dy, VDZP for the first coordination sphere, and VDZ for all other atoms).^{48,49} These 18 spin-free states are then mixed with SO coupling and the lowest 16 resulting states (${}^6H_{15/2}$ multiplet) are projected onto a crystal field (CF) Hamiltonian acting in the $(2J+1)$ -dimensional $|m_J\rangle$ basis.⁵⁰ The spin-phonon coupling Hamiltonian for each mode is evaluated using a linear vibronic coupling model, where we first determine the first derivatives of the CF parameters for each atomic Cartesian degree of freedom, then convert these into the normal mode basis using the appropriate linear-combination of atomic displacements from the normal mode vector.⁵⁰ This is done for all phonon modes, at all q -points in the sampling mesh.

Magnetic relaxation rates are determined using our code *Tau*, considering the Orbach and Raman-I rate expressions derived from perturbation theory,^{14,22} which are given by Equations 1–6 in the supporting information of Ref. ⁵⁰. Calculation of the Raman rates using these perturbative expressions requires an energy gap between the lowest Kramers doublet, which occurs in experiments due to the presence of a dipolar magnetic field and/or the driving AC magnetic field in the experiment, and thus we apply a magnetic field of 2 Oe along the main magnetic axis of the molecule, splitting the ground doublet by *ca.* 0.002 cm^{-1} . The Raman mechanism involves two phonons, with no restrictions on the energies and wavevectors, and the rate is obtained as the double-integral over pairs of modes.^{22,50} We restrict the domain of the phonon energies to $0 \leq \omega \lesssim \omega_{\text{cut}}$, where $\omega_{\text{cut}} = 267 \text{ cm}^{-1}$ is chosen as the minimum in the DoS above the low-energy pseudo-acoustic peak. The cut-off is applied to avoid divergences in the in the Raman-I rates (where the denominator of Equations 3–6 in the supporting information of Ref. ⁵⁰ would go zero when $\hbar\omega$ is resonant with a CF excitation), and is sufficiently smaller than the first crystal field excitation of 421 cm^{-1} . The double-integral is transformed into a one-dimensional integral due to the conservation of energy *via* the Dirac delta function, and is performed over anti-Lorentzian phonon lineshapes (Equation 7 in the supporting information of Ref. ⁵⁰) to an equivalent range of $\mu \pm 2\sigma$ (95%) using the trapezoidal

method with 40 equidistant steps; anti-Lorentzian lineshapes are used to ensure that the DoS goes exactly to zero at zero energy.

To assess the results of our solid-state calculations, we also calculated the spin-phonon coupling coefficients and magnetic relaxation rates for a gas-phase molecule of **1**. For that, we optimise the geometry of **1**, again with Dy replaced by Y, with Gaussian09d³⁹ using PBE-D3,^{34,35} the Stuttgart RSC 1997 ECP⁴¹⁻⁴³ for Y and the cc-pVDZ basis sets for all other atoms.

44

Results and discussion

Compound **1** is a monometallic Dy(III) molecule with a pentagonal bipyramidal coordination geometry. The molecule crystallises in the orthorhombic space group $C222_1$ with half a molecule in the asymmetric unit and two complete molecules in the conventional unit cell (Figure 1). Liu *et al.* report that compound **1** shows slow magnetic relaxation with $U_{\text{eff}} = 712 \text{ cm}^{-1}$ and $\tau_0 = 4.21 \times 10^{-12} \text{ s}$.²⁹ Optimisation of the crystal structure of **1** with periodic DFT yields a very similar structure to the experimental one used as the starting point: the optimised unit cell parameters are very similar to the measured values (Table S1), and the root-mean-square deviation (RMSD) for all the atomic positions (maximal overlap) is 0.10 Å. The low-energy phonon dispersion (Figure 2a) comprises the three acoustic modes (corresponding to rigid translations with zero energy at the Γ point) and a high density of dispersive pseudo-acoustic modes that arise predominantly from combinations of rigid molecular translations and rotations. Over the same region the DoS shows a high-density continuum of phonon modes below *ca.* 200 cm^{-1} (Figure 2b), while the complete spectrum extends up to 3500 cm^{-1} and at higher frequencies comprises relatively flat bands of intramolecular modes (Figure 2c).

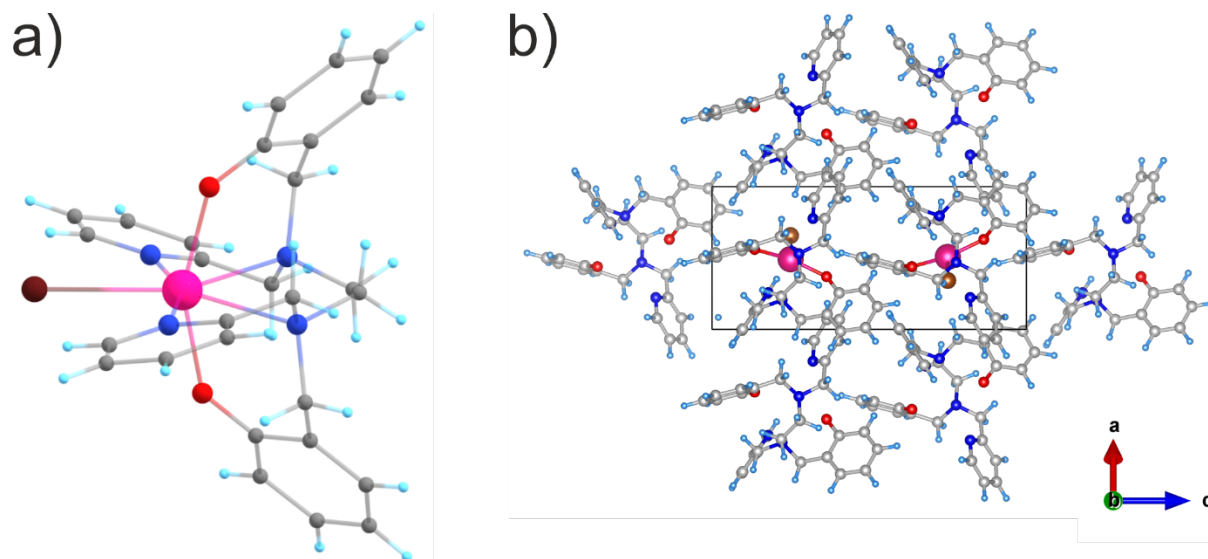


Figure 1. a) Molecular structure of **1** from X-Ray diffraction.²⁹ b) Optimised conventional unit cell containing two molecules of **1**. The atoms are colour coded as follows: Dy = pink, N = dark blue, Br = brown, O = red, C = grey, H = light blue.

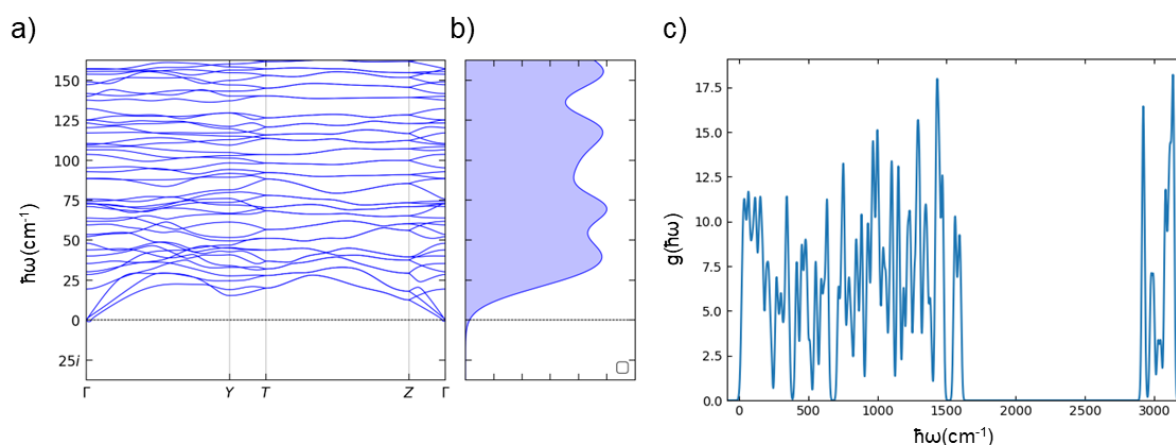


Figure 2. Calculated phonon spectrum for the crystal structure of **1**. a, b) Low-energy dispersion and density of states (DoS). c) Full energy range DoS. Both DoS plots are calculated using an $8 \times 8 \times 8$ q -point grid with Gaussian lineshapes and a 0.53 cm^{-1} FWHM linewidth.

Having determined the phonon spectrum of **1**, we then proceeded to calculate third-order (anharmonic) force constants and model the phonon-phonon interactions.²⁸ To obtain the lifetime τ_p and linewidths Γ , the phonon-phonon scattering processes are calculated explicitly for a grid of wavevectors in reciprocal space at a finite temperature (thermal occupation of the phonon modes are important for determining scattering). Here we have used $2 \times 2 \times 2$, $3 \times 3 \times 3$, $4 \times 4 \times 4$ and $5 \times 5 \times 5$ q -point grids (which have 6, 8, 21 and 27 unique q -points, respectively), and

performed the calculations at 10, 20, 30, 40, 50, 60 and 300 K. We find that calculated linewidths vary both as a function of wavevector and mode energy (Figure 3), but that the variation is relatively insensitive to the choice of grid (Figure S1). There is also a marked temperature dependence (Figures S2 and S3), which above 30 K is well approximated as $\Gamma \propto T$. In contrast, the high-temperature limit of Equation 1 is $\Gamma \propto T^2$ and the linewidths predicted by Equation 1 differ substantially from these *ab initio* calculations (Figure 3a). The calculated phonon linewidths for **1** at 300 K are on the order of 0.1-40 cm^{-1} (corresponding to lifetimes on the order of 100-0.1 ps, respectively), and some modes become much longer lived at low temperatures with lifetimes up to 4.5 ns (corresponding to linewidths of 0.001 cm^{-1}) at 10 K. This strong temperature dependence arises from the fact that with increasing temperature the phonons are more heavily populated, according to Bose-Einstein statistics, resulting in larger scattering probabilities.²⁸ Even this extremely long calculated lifetime is orders of magnitude shorter than the experimental spin lifetimes for this compound, which are seconds to hundreds of microseconds, justifying the commonly assumed Born-Markov approximation for molecular spin-dynamics.^{19,27} To the best of our knowledge the present study represents one of very few explicit calculations of the phonon linewidths and lifetimes for a molecular crystal, and the only such calculation for solid-state SMM.

The central quantity of interest for molecular spin-dynamics is the total DoS. Usually, the DoS is obtained using a chosen q -point grid and using arbitrary Gaussian or Lorentzian smoothing functions (e.g. Figure 3b). Here, because we have calculated the linewidths *ab initio*, we can directly calculate an *ab initio* DoS with no artificial smoothing functions (Figure 3c). The resulting low-energy DoS is sharply featured when using a small q -point grid (i.e. the $2 \times 2 \times 2$ q -point grid), but the low-energy DoS as $\omega \rightarrow 0$ (determined solely by the three acoustic modes) is expected to be quadratic in the frequency.⁵¹ The sharp features are due to the finite sum of q -points the Brillouin zone, and can be improved by using a larger grid to sample the dispersion of the modes more accurately (i.e. the $5 \times 5 \times 5$ q -point grid, though we note that this grid still does not fully capture the dispersion cf. Figure 3b). We note that using a small grid would be more problematic at lower temperatures given the drastic narrowing of the linewidths (Figure S4). Given the similar profiles of the linewidths obtained with different grids (Figure S1), the difference in the DoS obtained with the different q -point sampling in Figure 3b can be attributed to better integration of reciprocal space rather than to an improved accuracy of the calculated linewidths. We note that issues of a sharply-featured DoS can potentially be avoided

by using a fixed phonon linewidth of $\Gamma = 10 \text{ cm}^{-1}$, as this gives a smooth DoS even with a comparatively sparse $2 \times 2 \times 2$ q -point grid (Figure S5).

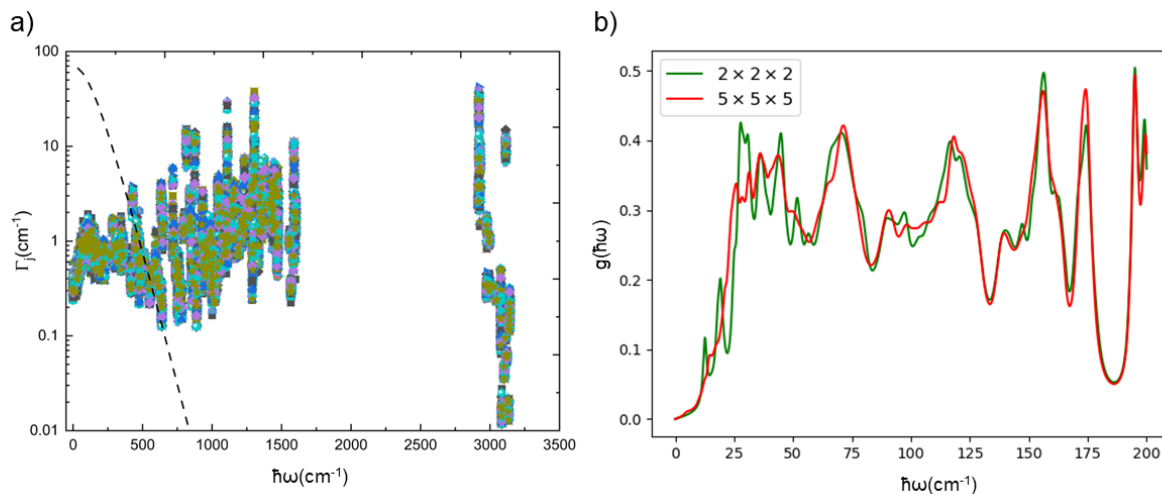


Figure 3. a) Phonon linewidths as a function of mode energy at 50 K for the 27 q points on a $5 \times 5 \times 5$ Brillouin zone sampling mesh; the different q points have differently coloured and shaped symbols. The dashed line shows the predictions from Equation 1. b) Low-energy DoS at 50 K constructed from the calculated frequencies and linewidths obtained on $2 \times 2 \times 2$ and $5 \times 5 \times 5$ q -point grids, using an anti-Lorentzian lineshape.

To examine the influence of calculated phonon linewidths on the spin dynamics, we proceeded to calculate the spin-phonon coupling and magnetic relaxation rates (see Methods). First, we examined the spin dynamics under the gas-phase ansatz by optimising the neutral molecule of **1** in the gas-phase, which yields an RMSD for all the atomic positions (maximal overlap) compared to the experimental crystal structure of 0.13 \AA . The calculated single-phonon magnetic relaxation rates for the Orbach mechanism, using the gas-phase vibrational modes and fixed linewidths show good agreement to the experimental data in the high-temperature Orbach region (Figure S6). As we have shown before, the absolute rates show a significant dependence on the choice of linewidth,^{10,19,24} with broader linewidths leading to faster relaxation rates. This behaviour occurs for single-phonon processes because there is only one possible energy that a phonon can have to cause a transition – $\hbar\omega = |E_f - E_i|$ (where E_f and E_i are the final and initial electronic state energies) – and a larger linewidth gives a larger probability that an overlap between $|E_f - E_i|$ and the set of calculated vibrational energies can occur. We find that the best agreement is obtained with $\Gamma = 1 \text{ cm}^{-1}$ (Figure S6), which is consistent with the approximate centre of the distribution of the calculated phonon linewidths at 300 K.

Two-phonon Raman rates can only be reliably obtained by considering the (pseudo-)acoustic phonons, in the solid-state, so this calculation cannot be performed using the gas-phase vibrational spectrum. We therefore also calculated the spin-phonon coupling and magnetic relaxation rates using the solid-state phonon modes generated using the set of supercell expansions commensurate with the q -point grids on which the calculated frequencies and linewidths were obtained (see Methods). To compare with the gas-phase calculations, we first performed calculations with fixed linewidths (i.e. disregarding the calculated Γ ; Figure S7). We again find that the single-phonon rates in the Orbach region are positively correlated with the choice of linewidth, but the dependence is far less significant than in the gas phase: the rates for $\Gamma = 0.1 \text{ cm}^{-1}$ and $\Gamma = 10 \text{ cm}^{-1}$ differ by 1.3 orders of magnitude at 60 K in the gas-phase calculations, but by significantly smaller values of 0.8, 0.9, 0.4 and 0.8 orders of magnitude for the phonon calculations with $2 \times 2 \times 2$, $3 \times 3 \times 3$, $4 \times 4 \times 4$ and $5 \times 5 \times 5$ q -point grids, respectively. Convergence toward the experimental data with respect to the size of the q -point grid is not continuous. In particular, we observe better convergence behaviour with “odd” versus “even” grids such that the $3 \times 3 \times 3$ grid improves over the $2 \times 2 \times 2$ grid, the $4 \times 4 \times 4$ grid gives less accurate results than the $3 \times 3 \times 3$ grid, and the largest $5 \times 5 \times 5$ grid improves over the $3 \times 3 \times 3$ grid (Figure S7). We attribute this to the inclusion/exclusion of the Brillouin-zone boundary points in the even/odd grids, and we would expect both types of grid to converge to the same result with higher sampling density, but our grids are clearly not yet in that limit. Overall, these results indicate that the choice of linewidth in the single-phonon Orbach region becomes less important when the solid-state phonons, rather than the gas-phase vibrations, are used with appropriate integration of the first Brillouin zone.

Calculating the two-phonon Raman rates with fixed linewidths shows that the calculated magnetic relaxation rates give the same temperature trend as in the experimental data but are *ca.* an order of magnitude faster (Figure S8). Counter-intuitively, and opposite to the behaviour of the single-phonon Orbach rates, the two-phonon Raman rates have a negative correlation with linewidth, i.e. the rates become slower with broader linewidths. This arises owing to the double-integral over the DoS containing terms such as (see Equations 3–6 in the supporting information of Ref. ⁵⁰) $\sum_{j \geq k} \iint \bar{n}(\hbar\omega)(\bar{n}(\hbar\omega') + 1)\rho_j(\hbar\omega)\rho_k(\hbar\omega')\delta(E_f - E_i - \hbar\omega + \hbar\omega')d\hbar\omega d\hbar\omega'$, where $\bar{n}(\hbar\omega)$ and $\bar{n}(\hbar\omega')$ are the Bose-Einstein occupations of the phonons, $\rho_j(\hbar\omega)$ and $\rho_k(\hbar\omega')$ are the anti-Lorentzian lineshape functions of the phonons centred at $\hbar\omega_j$ and $\hbar\omega_k$, respectively, and the integral is over the energies of the two phonons $\hbar\omega$ and $\hbar\omega'$. Here, the delta function (which enforces conservation of energy) allows many more pairs of

phonons to cause a transition between two states, because the difference in the phonon energy $-\hbar\omega + \hbar\omega'$ must match the difference in electronic state energy $E_f - E_i$. When the linewidths are larger, the phonons lines extend to higher energies, and the Bose-Einstein occupation factors strongly down-weight phonons at higher energies, hence reducing the magnitude of these contributions when the linewidths are larger.

As for the Orbach rates, we see that the dependence on the linewidth becomes smaller with improved reciprocal-space integration, and that the agreement with experiment improves with larger grids. However, the convergence with respect to q -point sampling is slower than for the single-phonon Orbach rates. Given that choosing a fixed $\Gamma = 10 \text{ cm}^{-1}$ results in a smooth DoS even for the $2 \times 2 \times 2$ grid (Figure S5), and the magnetic relaxation rates with the fixed linewidth also converge towards the experimental data as the grid density is increased (Figures S7 and S8), this means that improving the integration of the Brillouin zone does not merely generate a smooth DoS, but rather more accurately captures the dispersion of the spin-phonon couplings across the Brillouin zone. Given that we observed the same behaviour with the high-temperature Orbach rates, this strongly suggests that Γ -point-only spin-phonon coupling calculations are insufficient. We also note that the sensitivity of the magnetic relaxation rates in the Raman region to the phonon linewidth could provide an explanation for the correlation between crystalline disorder and the width of the distributions of magnetic relaxation rates,⁵² as well as the increase in the distribution in magnetic relaxation rates for this compound as the temperature is decreased; that is, the presence of crystalline disorder has more of an effect on the rates (i.e. increasing their distribution) as temperature is reduced where the Raman relaxation mechanism dominates.

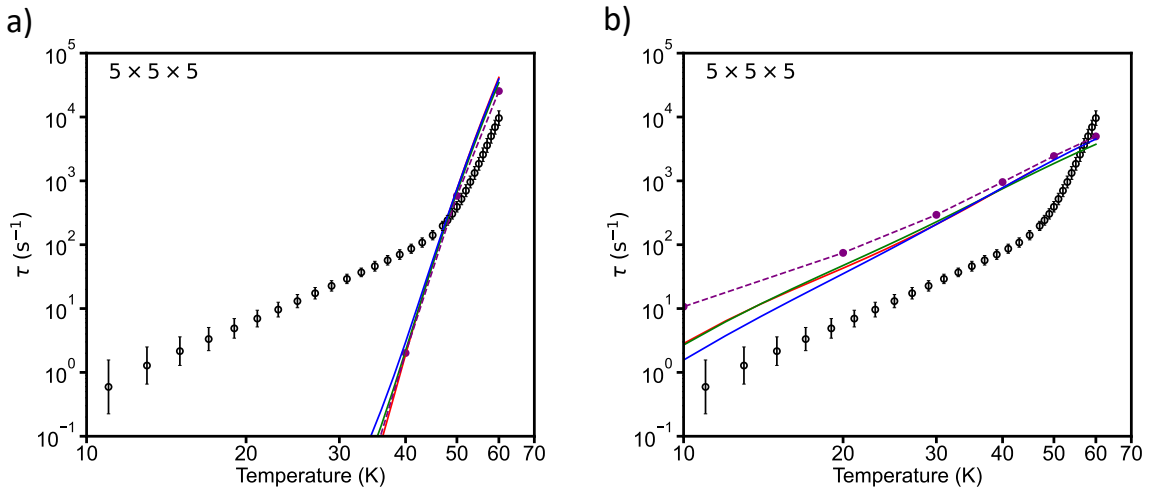


Figure 4. Experimental (black circles) and calculated magnetic relaxation rates for **1**. Calculations are performed using the solid-state phonon modes on $5 \times 5 \times 5$ grid, considering single- (a) and two-phonon (b) mechanisms, with a fixed $\Gamma = 10 \text{ cm}^{-1}$ (blue), linewidths predicted by Equation 1 (red), mode-dependent calculated linewidths at 300 K (green), and calculated mode- and temperature-dependent linewidths (purple points and dashed lines). The error bars on the experimental data points denote one estimated standard deviation of the distribution of relaxation rates.⁵²

We now examine the impact of using the calculated phonon linewidths. In the Orbach region, the rates obtained using mode- and temperature-dependent linewidths coincide with the fixed linewidth calculations using $\Gamma = 10 \text{ cm}^{-1}$ (Figures 4 and S7). For the Raman region, the rates with calculated linewidths are close to those calculated with the fixed $\Gamma = 10 \text{ cm}^{-1}$ at 60 K, but increasingly approach the smaller fixed-linewidth calculations at lower temperature, crossing the $\Gamma = 0.1 \text{ cm}^{-1}$ rates between 20 and 10 K (Figures 4 and S8). As the Raman rates are more strongly affected by the choice of linewidth than the Orbach rates, it is unsurprising that the extreme narrowing of some of the calculated phonon linewidths at low temperatures has a marked impact on the temperature-dependent relaxation rates. However, we note that the profile of the rates calculated using mode- and temperature-dependent linewidths does not agree with the experimental data at the lowest temperatures, and in particular, they appear to level-off while the experimental rates continue to decrease. Hence, we suggest that the extreme narrowing of the calculated linewidths at low temperatures is overestimated, and that there are likely other sources of phonon scattering (such as boundary effects, impurities, defects and/or disorder) in real crystals that would lead to shorter phonon lifetimes and therefore broader linewidths than estimated by our DFT calculations on a perfect infinite crystal.

Finally, we compared our results to the effective NVT phonon linewidth proposed by Lunghi *et al.* (Equation 1). We find that in both the Orbach and Raman regions this expression gives rates that are close to the fixed $\Gamma = 10 \text{ cm}^{-1}$ curves (Figures 4, S9 and S10), and, in fact, gives rates nearly identical to those obtained using calculated linewidths at 300 K, which agree well with the *ab initio* linewidth results at high temperature. However, the phonon linewidths predicted for the low-energy phonons using this function increase drastically at high temperature such that the numerical integration over the anti-Lorentzian phonon lineshapes in the two-phonon Raman mechanism becomes difficult, and we therefore only present these data for $T \leq 46 \text{ K}$.

Overall, it appears that considering the solid-state phonons, as compared to gas-phase vibrations, along with a dense sampling of reciprocal space is important. However, that the choice of phonon linewidth model is not crucial. Indeed, due to the likely unphysical narrowing of calculated phonon linewidths at very low temperature, and the similar results obtained using the calculated 300 K and temperature-dependent linewidths, we do not suggest using temperature-dependent *ab initio* linewidths. Furthermore, owing to the large computational burden of calculating *ab initio* linewidths and their similarity to the NVT approximation, we suggest that calculation of linewidths is not worth the effort. Finally, considering the difficulties with numerical integration using the NVT linewidths and their huge energy dependence (Figure 3a), and yet the similarity of the results to calculations with a fixed $\Gamma = 10 \text{ cm}^{-1}$, we suggest that the simple fixed-linewidth method is the most transferrable and economic for molecular spin-dynamics calculations.

Conclusions

We have performed *ab initio* calculations of the phonon lifetimes and linewidths for a single-molecule magnet in its molecular crystalline phase. We find that the calculated linewidths deviate from the approximate model derived from the NVT canonical ensemble and have a significant dependence on the mode energy, phonon wavevector, and temperature. However, *ab initio* calculations of the spin-phonon coupling and spin dynamics show that the choice of linewidth model (fixed, NVT, or fully *ab initio*) is less important than the density of the integration grid used to sample the phonon Brillouin zone, which is required to capture the intrinsic dispersion of the spin-phonon coupling strengths. Hence, we advise that solid-state phonon calculations with dense grids should be used in conjunction with either the NVT approximation for the phonon linewidths or a fixed linewidth on the order of $\Gamma = 10 \text{ cm}^{-1}$ for accurate and efficient spin dynamics calculations.

Acknowledgements

We thank the Royal Society for a University Research Fellowship (URF191320 to NFC), UK Research and Innovation for a Future Leaders Fellowship (MR/T043121/1 to JMS), the European Research Council for a Starting Grant (StG- 851504 to NFC), and the Computational

Shared Facility at The University of Manchester for access to computational resources. *Via* our membership of the UK's HEC Materials Chemistry Consortium, which is funded by the UK Engineering and Physical Sciences Research Council (EP/R029431), this work used the ARCHER2 UK National Supercomputing Service (<https://www.archer2.ac.uk>). Raw data supporting this publication have been deposited on FigShare (doi: 10.48420/22148963).

References

- 1 D. Gatteschi, R. Sessoli and J. Villain, *Molecular Nanomagnets*, Oxford University Press, 2006.
- 2 N. F. Chilton, *Annu. Rev. Mater. Res.*, 2022, **52**, 79–101.
- 3 R. Sessoli, *Nature*, 2017, **548**, 400–401.
- 4 M. N. Leuenberger and D. Loss, *Nature*, 2001, **410**, 789–793.
- 5 A. Gaita-Ariño, F. Luis, S. Hill and E. Coronado, *Nat. Chem.*, 2019, **11**, 301–309.
- 6 L. Bogani and W. Wernsdorfer, *Nat. Mater.*, 2008, **7**, 179–186.
- 7 L. Escalera-Moreno, J. J. Baldoví, A. Gaita-Ariño and E. Coronado, *Chem. Sci.*, 2018, **9**, 3265–3275.
- 8 A. Lunghi and S. Sanvito, *J. Phys. Chem. Lett.*, 2020, **11**, 6273–6278.
- 9 M. Shiddiq, D. Komijani, Y. Duan, A. Gaita-Ariño, E. Coronado and S. Hill, *Nature*, 2016, **531**, 348–351.
- 10 C. A. P. Goodwin, F. Ortu, D. Reta, N. F. Chilton and D. P. Mills, *Nature*, 2017, **548**, 439–442.
- 11 A. Lunghi, F. Totti, S. Sanvito and R. Sessoli, *Chem. Sci.*, 2017, **8**, 6051–6059.
- 12 A. Abragam and B. Bleaney, *Electron Paramagnetic Resonance of Transition Ions*, Oxford University Press, 1970.
- 13 A. Chiesa, F. Cugini, R. Hussain, E. Macaluso, G. Allodi, E. Garlatti, M. Giansiracusa, C. A. P. Goodwin, F. Ortu, D. Reta, J. M. Skelton, T. Guidi, P. Santini, M. Solzi, R. De Renzi, D. P. Mills, N. F. Chilton and S. Carretta, *Phys. Rev. B*, 2020, **101**, 174402.
- 14 K. N. Shrivastava, *Phys. Status Solidi B*, 1983, **117**, 437–458.
- 15 L. T. A. Ho and L. F. Chibotaru, *Phys. Rev. B*, 2018, **97**, 024427.
- 16 F.-S. Guo, B. M. Day, Y.-C. Chen, M.-L. Tong, A. Mansikkamäki and R. A. Layfield, *Science*, 2018, **362**, 1400–1403.
- 17 C. A. Gould, K. R. McClain, D. Reta, J. G. C. Kragsskow, D. A. Marchiori, E. Lachman, E.-S. Choi, J. G. Analytis, R. D. Britt, N. F. Chilton, B. G. Harvey and J. R. Long, *Science*, 2022, **375**, 198–202.
- 18 K. R. McClain, C. A. Gould, K. Chakarawet, S. Teat, T. J. Groshens, J. R. Long and B. G. Harvey, *Chem. Sci.*, 2018, **9**, 8492–8503.
- 19 D. Reta, J. G. C. Kragsskow and N. F. Chilton, *J. Am. Chem. Soc.*, 2021, **143**, 5943–5950.
- 20 A. Lunghi and S. Sanvito, *J. Phys. Chem. C*, 2020, **124**, 5802–5806.
- 21 L. Escalera-Moreno, N. Suaud, A. Gaita-Ariño and E. Coronado, *J. Phys. Chem. Lett.*, 2017, **8**, 1695–1700.
- 22 A. Lunghi, *Sci. Adv.*, 2022, **8**, eabn7880.
- 23 A. Lunghi, F. Totti, R. Sessoli and S. Sanvito, *Nat. Commun.*, 2017, **8**, 14620.
- 24 P. Evans, D. Reta, G. F. S. Whitehead, N. F. Chilton and D. P. Mills, *J. Am. Chem. Soc.*, 2019, **141**, 19935–19940.

- 25K.-X. Yu, J. G. C. Kragsskow, Y.-S. Ding, Y.-Q. Zhai, D. Reta, N. F. Chilton and Y.-Z. Zheng, *Chem*, 2020, **6**, 1777–1793.
- 26A. Albino, S. Benci, L. Tesi, M. Atzori, R. Torre, S. Sanvito, R. Sessoli and A. Lunghi, *Inorg. Chem.*, 2019, **58**, 10260–10268.
- 27M. Briganti, F. Santanni, L. Tesi, F. Totti, R. Sessoli and A. Lunghi, *J. Am. Chem. Soc.*, 2021, **143**, 13633–13645.
- 28A. Togo, L. Chaput and I. Tanaka, *Phys. Rev. B*, 2015, **91**, 094306.
- 29J. Liu, Y.-C. Chen, J.-L. Liu, V. Vieru, L. Ungur, J.-H. Jia, L. F. Chibotaru, Y. Lan, W. Wernsdorfer, S. Gao, X.-M. Chen and M.-L. Tong, *J. Am. Chem. Soc.*, 2016, **138**, 5441–5450.
- 30G. Kresse and J. Hafner, *Phys. Rev. B*, 1993, **47**, 558–561.
- 31G. Kresse and J. Hafner, *Phys. Rev. B*, 1994, **49**, 14251–14269.
- 32G. Kresse and J. Furthmüller, *Comput. Mater. Sci.*, 1996, **6**, 15–50.
- 33G. Kresse and J. Furthmüller, *Phys. Rev. B*, 1996, **54**, 11169–11186.
- 34J. P. Perdew, K. Burke and M. Ernzerhof, *Phys. Rev. Lett.*, 1996, **77**, 3865–3868.
- 35S. Grimme, J. Antony, S. Ehrlich and H. Krieg, *J. Chem. Phys.*, 2010, **132**, 154104.
- 36G. Kresse and J. Hafner, *J. Phys. Condens. Matter*, 1994, **6**, 8245.
- 37G. Kresse and D. Joubert, *Phys. Rev. B*, 1999, **59**, 1758–1775.
- 38A. Togo and I. Tanaka, *Scr. Mater.*, 2015, **108**, 1–5.
- 39M. J. Frisch, G. W. Trucks, H. B. Schlegel, G. E. Scuseria, M. A. Robb, J. R. Cheeseman, G. Scalmani, V. Barone, B. Mennucci, G. A. Petersson, H. Nakatsuji, M. Caricato, X. Li, H. P. Hratchian, A. F. Izmaylov, J. Bloino, G. Zheng, J. L. Sonnenberg, M. Hada, M. Ehara, K. Toyota, R. Fukuda, J. Hasegawa, M. Ishida, T. Nakajima, Y. Honda, O. Kitao, H. Nakai, T. Vreven, J. A. Montgomery Jr., J. E. Peralta, F. Ogliaro, M. Bearpark, J. J. Heyd, E. Brothers, K. N. Kudin, V. N. Staroverov, T. Keith, R. Kobayashi, J. Normand, K. Raghavachari, A. Rendell, J. C. Burant, S. S. Iyengar, J. Tomasi, M. Cossi, N. Rega, J. M. Millam, M. Klene, J. E. Knox, J. B. Cross, V. Bakken, C. Adamo, J. Jaramillo, R. Gomperts, R. E. Stratmann, O. Yazyev, A. J. Austin, R. Cammi, C. Pomelli, J. W. Ochterski, R. L. Martin, K. Morokuma, V. G. Zakrzewski, G. A. Voth, P. Salvador, J. J. Dannenberg, S. Dapprich, A. D. Daniels, Ö. Farkas, J. B. Foresman, J. V. Ortiz, J. Cioslowski and D. J. Fox, Gaussian 09, Revision D.01, Gaussian, Inc., Wallingford CT, 2013.
- 40C. M. Breneman and K. B. Wiberg, *J. Comput. Chem.*, 1990, **11**, 361–373.
- 41W.-T. Chan and R. Fournier, *Chem. Phys. Lett.*, 1999, **315**, 257–265.
- 42Á. Valdés *, R. Prosimi, P. Villarreal and G. Delgado-Barrio, *Mol. Phys.*, 2004, **102**, 2277–2283.
- 43M. Lei, N. Wang, L. Zhu and H. Tang, *Chemosphere*, 2016, **150**, 536–544.
- 44T. H. Dunning, *J. Chem. Phys.*, 1989, **90**, 1007–1023.
- 45I. Fdez. Galván, M. Vacher, A. Alavi, C. Angeli, F. Aquilante, J. Autschbach, J. J. Bao, S. I. Bokarev, N. A. Bogdanov, R. K. Carlson, L. F. Chibotaru, J. Creutzberg, N. Dattani, M. G. Delcey, S. S. Dong, A. Dreuw, L. Freitag, L. M. Frutos, L. Gagliardi, F. Gendron, A. Giussani, L. González, G. Grell, M. Guo, C. E. Hoyer, M. Johansson, S. Keller, S. Knecht, G. Kovačević, E. Källman, G. Li Manni, M. Lundberg, Y. Ma, S. Mai, J. P. Malhado, P. Å. Malmqvist, P. Marquetand, S. A. Mewes, J. Norell, M. Olivucci, M. Oppel, Q. M. Phung, K. Pierloot, F. Plasser, M. Reiher, A. M. Sand, I. Schapiro, P. Sharma, C. J. Stein, L. K. Sørensen, D. G. Truhlar, M. Ugandi, L. Ungur, A. Valentini, S. Vancoillie, V. Veryazov, O. Weser, T. A. Wesolowski, P.-O. Widmark, S. Wouters, A. Zech, J. P. Zobel and R. Lindh, *J. Chem. Theory Comput.*, 2019, **15**, 5925–5964.
- 46M. Reiher, *Theor. Chem. Acc.*, 2006, **116**, 241–252.

- 47F. Aquilante, L. Gagliardi, T. B. Pedersen and R. Lindh, *J. Chem. Phys.*, 2009, **130**, 154107.
- 48B. O. Roos, R. Lindh, P.-Å. Malmqvist, V. Veryazov and P.-O. Widmark, *J. Phys. Chem. A*, 2005, **109**, 6575–6579.
- 49B. O. Roos, R. Lindh, P.-Å. Malmqvist, V. Veryazov and P.-O. Widmark, *J. Phys. Chem. A*, 2004, **108**, 2851–2858.
- 50J. K. Staab and N. F. Chilton, *J. Chem. Theory Comput.*, 2022, **18**, 6588–6599.
- 51M. T. Dove, *Introduction to lattice dynamics*, Cambridge University Press, Cambridge ; New York, 1993.
- 52D. Reta and N. F. Chilton, *Phys. Chem. Chem. Phys.*, 2019, **21**, 23567–23575.